Growth and characterization of β-Mn structured CoZn thin films

M. Dearg [1,*,†] G. Burnell [1] S. Langridge [2] and C. H. Marrows [1,‡]
[1]*School of Physics and Astronomy, University of Leeds, Leeds LS2 9JT, United Kingdom*
[2]*ISIS Neutron and Muon Source, STFC Rutherford Appleton Laboratory, Didcot, Oxon. OX11 0QX, United Kingdom*

(Received 20 November 2023; revised 23 May 2025; accepted 11 June 2025; published 7 July 2025)

Thin films of polycrystalline β-Mn structure CoZn have been grown on thermally oxidized Si substrates by cosputtering from elemental targets followed by annealing. A range of films grown with variable Co deposition power and fixed Zn deposition power was produced, so as to vary the proportions of the two elements reaching the substrate, which were annealed postgrowth. While all films exhibited a (221) β-Mn structure CoZn texture in x-ray diffraction, transmission electron microscopy showed that the composition with the highest integrated intensity for that Bragg peak contained large voids and was covered by a thick ZnO cap owing to being Co deficient overall. CoZn films deposited at ratios tuned to give the optimal volume fraction of β-Mn were continuous, with crystallites up to 200 nm in size, with a much thinner ZnO cap layer. Magnetic measurements show that such optimal CoZn films have a Curie temperature $T_C \sim 420$ K and saturation magnetization of 120 emu/cm^3, properties close to those reported for bulk crystals. Excess Co beyond this point leads to a significant retained ferromagnetism above the Curie point of the CoZn, suggesting Co-rich aggregates. The β-Mn structure is chiral ($P4_132/P4_332$ space group) and is known to give rise to a Dzyaloshinkii-Moriya interaction (DMI) that stabilizes room-temperature skyrmions in the bulk. Our thin films are thus a potential materials platform, compatible with planar processing technology, for magnetic skyrmions arising from a bulk DMI.

DOI: 10.1103/rfjk-km1b

I. INTRODUCTION

Magnetic skyrmions, topologically nontrivial magnetization textures with particle-like properties, hold potential for data storage due to their topological stability, nanometric size, and low driving-current densities [1–3]. Long predicted as arising in magnets with chiral interactions [4], they were first observed in MnSi [5], which possesses the B20 lattice structure. This chiral lattice gives rise to a bulk Dzyaloshinskii-Moriya interaction (DMI) that stabilizes the skyrmions. Skyrmions were subsequently observed in other B20 compounds such as $Fe_{1-x}Co_xSi$ [6], FeGe [7], and Cu_2OSeO_3 [8]. Nevertheless, these widely studied B20 skyrmion materials present a bottleneck to applications, owing to the fact that they only exhibit magnetic order below room temperature [9].

By revisiting noncentrosymmetric crystals reported to be ferromagnetic above room temperatures, a new class of material was discovered to host skyrmions above room temperature [10]. CoZnMn alloys have long been known to host a β-Mn phase [11–14]. The β-Mn structure, named for the second allotrope of Mn, refers to the cubic space-group numbers 212 and 213, which represent the chiral handedness due to the enantiomorphic nature of point group 432 [15]. The β-Mn–type structure forms a primitive cubic of space group $P4_332$ or $P4_132$ depending on handedness (shown in Fig. 1), which consists of 20 atoms split across the inequivalent crystallographic 8*c* and 12*d* sites [16]. This structure breaks spatial inversion symmetry, the condition required for a bulk DMI to manifest itself. Such alloys were shown to exhibit DMI-stabilized skyrmions at and above room temperature in bulk [10], with a rich variety of properties subsequently discovered [9,17–22].

This makes such β-Mn structure alloys candidates for developing room-temperature skyrmion technologies based on bulk DMI, alongside magnetic multilayer systems that possess interfacial DMI [23–29]. Thin-film materials are needed for compatibility with the planar processing methods used in the microelectronics industry, as well as to offer the possibility of strain engineering the skyrmion state [30]. While the multilayer systems are already in this form, β-Mn structure CoZn-based alloys have only been studied as bulk crystals to date.

Here, we show the development of a cosputter deposition and postgrowth annealing protocol capable of yielding CoZn films with the desired β-Mn crystal structure. Since the films are grown on the amorphous SiO_x surface of thermally oxidized Si wafer, they are polycrystalline, albeit with large grains and a strong (221) texture. We emphasize the importance of correctly balancing the sputter fluxes of Co and Zn reaching the substrate. The high mobility of Zn means that

*Present address: School of Physics, Engineering and Technology, University of York, York YO10 5DD, United Kingdom.
†Contact author: malcolm.dearg@york.ac.uk
‡Contact author: c.h.marrows@leeds.ac.uk

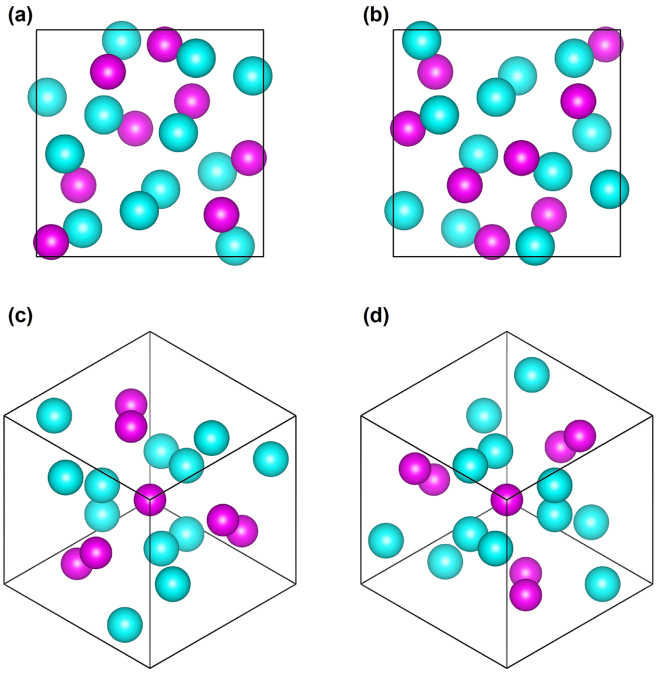

FIG. 1. Crystallographic visualization of the β-Mn structure $P4_132$ and $P4_332$ space groups, for a 293 K CoZn alloy of lattice constant 6.33 Å, and equivalent isotropic displacement [*x, y, z*] parameters for 8*c* (magenta) and 12*d* (cyan) Wyckoff sites of [0.0648, 0.0648, 0.0648] and [0.125, 0.2030, 0.4530], respectively [14]. (a), (c) [100] and [111] orientations of $P4_132$, respectively. (b), (d) [100] and [111] orientations of $P4_332$, respectively. The two chiral forms are obtained by inverting the position of all of the atoms with respect to the center of the unit cell. In (a) and (b), the height of the atom is represented by the size of the sphere drawn to represent it. Visualizations were produced using VESTA [31].

excess Zn segregates to the surface of the film and oxidizes, forming a ZnO capping layer, leaving behind voids for Zn-rich growth. On the other hand, Co-rich growth leads to a weakly temperature-dependent background magnetization that we attribute to Co aggregates. For optimally balanced growth the films are smooth, contain large crystallites ∼200 nm in lateral size, and exhibit magnetic order well above room temperature, with a Curie point of about 420 K.

II. EXPERIMENTAL METHODS

A. Sputtering

Samples of thin-film CoZn were deposited by cosputtering from elemental targets, with the final film composition controlled by setting the ratio of sputter powers applied to the targets. These films were grown on the ∼100-nm SiO_x surface layer of 0.5-mm-thick thermally oxidized Si substrates, which were at ambient temperature inside the vacuum chamber. The deposition was done using balanced magnetrons with an argon working gas at a growth pressure of 3.2 mTorr. The growth system used has a base pressure of approximately 1×10^{-8} Torr.

B. Annealing

The samples were isolated for annealing postgrowth by sealing in quartz glass ampules under a vacuum. The tube was evacuated to a roughing pressure of order $10^{-1} \sim 10^{-2}$ Torr before applying heat to the tube with an oxyacetylene torch until it was fully sealed, then twisted by hand until the ampule containing the samples was sealed and separated from the main tube body. At every step in the process the system was repeatedly pump purged with 99.9999%-pure argon gas to keep the sample atmospheric environment as free from oxygen as possible.

Annealing was performed using a muffle furnace with a proportional-integral-derivative (PID) temperature controller; temperature measurement was by a K-type thermocouple. The furnace is a single-piece molded ceramic fiber chamber for high thermal efficiency, with heating elements embedded inside the walls of the chamber. Sample temperature stability in the chamber at rated temperature in thermal steady state is within ±1 °C, with a temperature uniformity of ±10 °C, up to a maximum temperature of 1100 °C.

The temperature controller used allows for up to four setpoints of ramp rate, temperature, and dwell time to be defined, illustrated schematically in Fig. 2(a). In the case of the samples described here, the typical annealing profile was to use staggered (decreasing) ramp rates ($R1/R2/R3$) of 5/3/1 °C to temperature setpoints ($T1/T2/T3$) of 300/350/400 °C and a final-stage dwell time $D3$ of 48 h. After annealing, samples were either cooled at the natural rate of the furnace with the heating output turned off, or quenched in water ($R4$). Occasionally, intermittent dwell times ($D1/D2$) were used at the 300/350 °C temperature setpoints of up to 48 h. These examples are of the typical process; other values for these parameters were explored in improving the quality (crystalline order and magnetic properties) of films.

C. X-ray diffraction

X-ray-diffraction (XRD) studies were performed using a diffractometer of Bragg-Brentano geometry with a 9-kW rotating Cu anode x-ray source. Monochromatic K_α radiation was achieved using a Ge (220) two-bounce monochromator, and divergence limited with 5° receiving Soller slits. The expected XRD patterns from β-Mn structure CoZn and ZnO are shown in Fig. 3.

D. Electron microscopy and energy-dispersive x-ray spectroscopy analysis

Imaging of the sample surface and production of lamella cross-section specimens were conducted using a dual-beam focused ion-beam/scanning electron microscope (FIB/SEM) instrument. Scanning electron microscopy was performed with an accelerating voltage of 5 kV. Lamella cross sections were prepared from thin-film samples following the standard "lift-out" process [35–37]. The lamellae are estimated to be <100 nm thick.

Transmission electron microscopy (TEM) and scanning TEM (STEM) were performed on an aberration-corrected microscope with a 300-kV extreme field-emission gun source, with the beam monochromated to an energy spread of

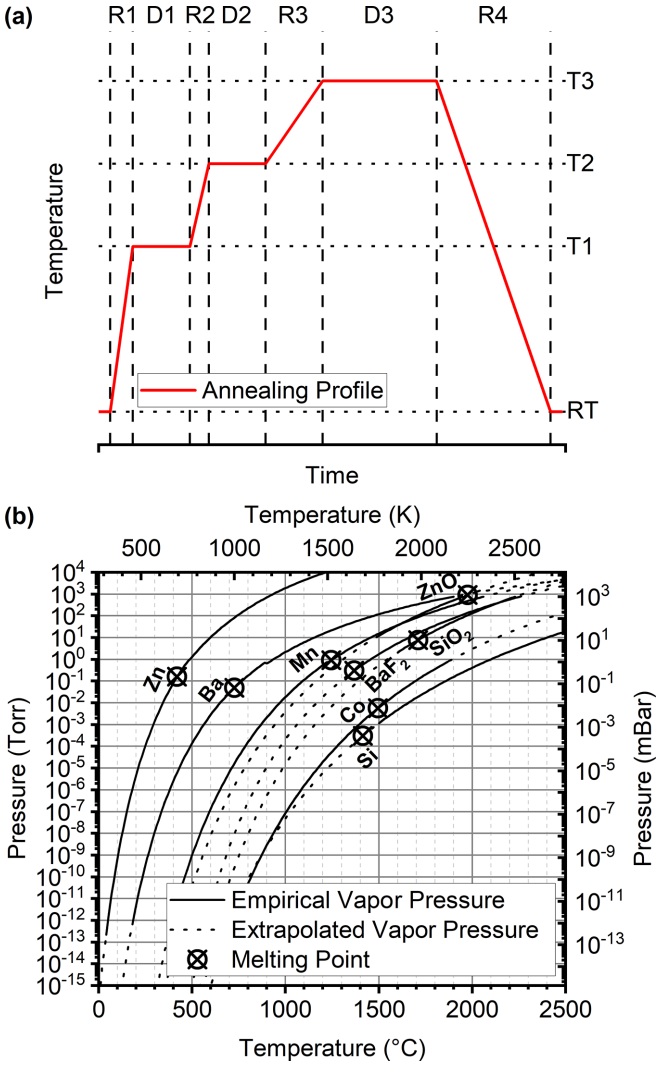

FIG. 2. Annealing. (a) General annealing profile schematic. The temperature axis defines temperature set-points ($T1$, $T2$, etc.) above room temperature (RT), while the time axis shows representations for the various dwell (D) and ramp (R) periods. (b) Vapor-pressure curves for elements and compounds pertinent to this work. These curves were generated from the Antoine coefficients and the Antoine equation [32,33], expressed as $\log_{10}(P) = A - \frac{B}{T+C}$, where P is pressure, A, B, and C are the Antoine coefficients, and T is the temperature.

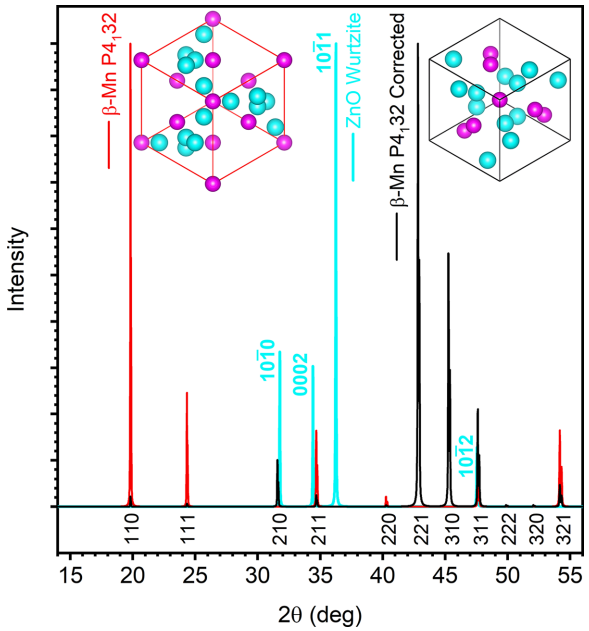

FIG. 3. Simulation of the x-ray powder-diffraction pattern for the β-Mn space group $P4_332/P4_132$ (space-group number 212/213). After accounting for the equivalent isotropic displacement parameters for the 8c and 12d sites [14], the brightest expected reflection shifts from the {110} in the basic space group (red), to the {221} in the corrected structure (black). The other major component seen in the films herein, ZnO (cyan) [34], shows a number of overlapping peaks with the CoZn β-Mn phase. Structures and simulated data here were produced in VESTA [31].

~0.25 eV. High-resolution TEM (HRTEM), bright-field (BF) and high-angle annular dark-field (HAADF-STEM) imaging modes were used. Energy-dispersive x-ray spectroscopy (EDXS) was performed with the same microscope.

E. Magnetometry

Magnetometry was performed using a superconducting quantum interference device vibrating sample magnetometer (SQUID-VSM), equipped with a 7-T superconducting solenoid magnet, capable of heating the sample up to 1000 K under a pressure <100 mTorr.

Our measurement protocol began with an isothermal hysteresis loop $M(H)$ measurement at room temperature from positive to negative saturating field $\pm H_{\max} = 8000$ Oe and back to positive before returning to a measurement field of $H_{\text{measure}} = +50$ Oe. This field was then held constant at this value while the temperature was raised to 500 K in order to measure $M(T)$. A further $M(H)$ hysteresis loop was performed at this elevated temperature, which was expected to be above the Curie point T_C of the CoZn but at which any Co regions would still be strongly ferromagnetic. Fields were applied in the plane of the sample in all cases.

$M(T)$ curves were fitted from $T = 300$ K to the Curie temperature $T = T_C$ with an empirical expression that approximates to Bloch's law at low T [38], written as

$$M(T) = M_{300} \times \left(1 - \left[\frac{T}{T_C}\right]^{\alpha}\right)^{\beta}, \tag{1}$$

where M_{300} is the magnetization at room temperature, α is an exponent representing the "Bloch" term describing the behavior in the low-temperature region, and β is an exponent representing the "Curie" term describing the behavior near the Curie point.

III. RESULTS

A. Sample growth and x-ray diffraction

XRD was used to analyze the crystallographic properties of the films that we grew. To produce samples of varied composition, we cosputtered films while varying the Co power between samples with the Zn sputter power fixed at 25 W [39].

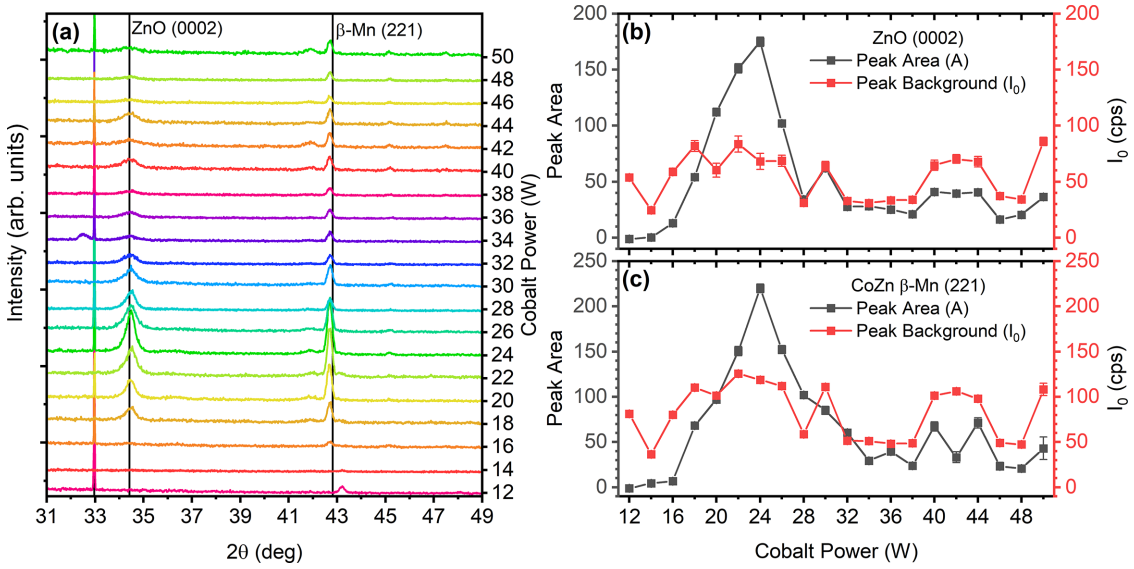

FIG. 4. XRD analysis of postannealed sputtered CoZn thin films. (a) XRD patterns for films deposited with various values of Co sputter power (Zn fixed at 25 W). Principal peaks are (002) ZnO at ∼34.45° and (221) β-Mn at ∼42.70°. The expected positions for these are marked by solid black lines. Weaker peaks can be seen at ∼45.2° and ∼47.5°, which correspond to expected positions for (310) and (311) β-Mn, respectively. The sharp peak at ∼32.96° is the classically "forbidden" (200) peak of Si. Samples here are calibrated to all fall in the range 400–500-Å thick. (b) Summary of Gaussian peak fitting results for the ZnO (002) peak. (c) Summary of Gaussian peak fitting results for the β-Mn (221) peak.

A postgrowth annealing protocol consistent with Fig. 2(a) was developed on the basis of a broader range of XRD studies to optimize the presence of Bragg reflections corresponding to the β-Mn structure while minimizing those corresponding to other phases. The films were all 40–50-nm thick in total, with a gradual variation with sputter power, decreasing in thickness as the Co power rose.

Our XRD studies have also shown a tendency for zinc to be vaporized from the surface of the films for annealing temperatures over 500 °C, resulting in emerging pure cobalt-phase Bragg peaks. This is due to the high vapor pressure of zinc at these temperatures [see Fig. 2(b)].

Following this preliminary work, we acquired XRD patterns for our series of annealed, cosputtered films, shown in Fig. 4(a). Comparison with Fig. 3 shows that most balances of sputter powers, but especially for a Co sputter power around 24 W, yield peaks primarily around 34.45° and 42.70°. These peaks were determined to be the (002) (34.4201°) and (221) (42.8237°) reflections of ZnO and β-Mn structure CoZn, respectively, by comparison against all known allotropes and alloy phases of cobalt, zinc, and their oxides. Since {221} are close-packed planes for the β-Mn structure, this is the expected orientation for textured films of CoZn.

There are indications of a correlation of the appearance and ordering of ZnO with the β-Mn. Figures 4(b) and 4(c) show the results of fitting the two peaks with a Gaussian, where I_0 is the background intensity and A is integrated intensity under the peak.

It can be seen from Figs. 4(b) and 4(c) that the integrated intensity of both the ZnO and β-Mn CoZn rise and fall together. This would indicate some correlated behavior even when minimizing the free Zn at higher Co weighting. Since, as we shall see later, the ZnO forms as a cap on top of the CoZn, the correlation we observe here is one that might reasonably be expected: a better crystallographically oriented underlayer is likely to lead to a better-oriented capping layer.

Furthermore, the I_0 term also rises and falls in the same manner, which will to some degree be suppressing the integrated intensity under the peak and thus the prominence of the two distinct peaks found in the series. This elevation of the I_0 term also indicates that the broadening of the peak becomes non-Gaussian towards the base, which implies that there is a distribution of smaller disordered crystallites.

Since the β-Mn (221) peak is strongest for 24-W Co deposition power, we began our investigations in films grown in that way.

B. Electron microscopy

Figure 5(a) shows a preliminary SEM image of the surface of the 24:25-W Co:Zn sample taken in the FIB/SEM system prior to laying down the protective coatings needed for preparing the cross-section specimen. This power ratio is the one at which the strongest XRD peak for β-Mn structure CoZn is observed. The contrast is not uniform, indicating an inhomogeneous surface. Further investigation, by cross-section HAADF-STEM imaging of a lamella taken from a similar region [Fig. 5(b)] shows there to be large voids within the film. While the XRD shows that the CoZn material is highly ordered in the β-Mn structure at this 24:25-W Co:Zn composition, the excess of zinc at high temperatures and low pressures leads to the vaporization of zinc, causing these large voids to form. The distribution of O, Zn, and Co around these voids is shown in the EDXS maps in Figs. 5(c)–5(e), respectively. The EDXS maps reveal a ZnO layer that persists as a cap across the void site, while there is almost no cobalt

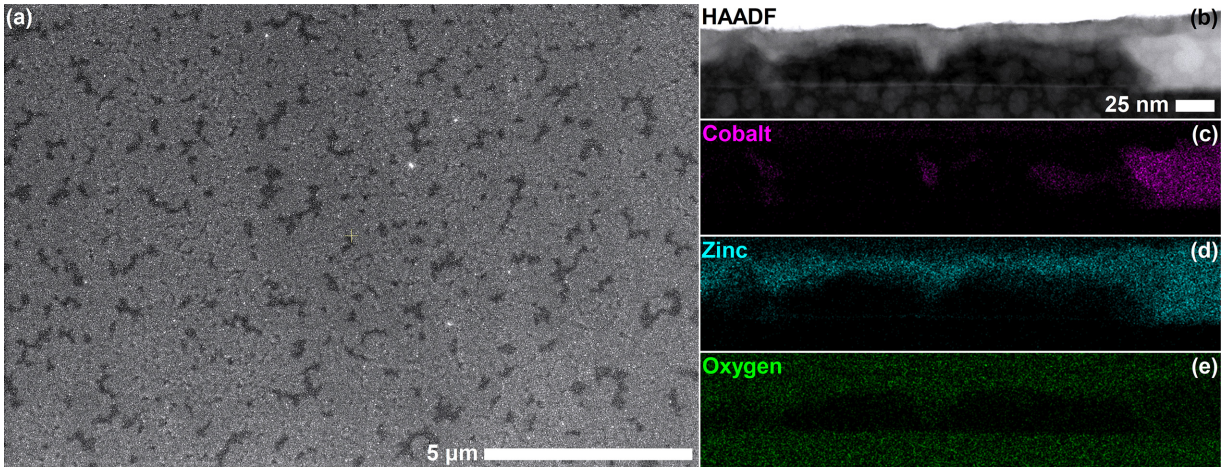

FIG. 5. Electron microscopy of an annealed sample of 24:25-W Co:Zn (approximately 470 ± 20 Å thick). (a) SEM image taken normal to the sample surface showing contrast differences within the layer. (b) HAADF-STEM image of an extracted lamella cross section, which reveals the surface contrast to be due to large voids. Breakdown of the composite elements expected within the EDXS image around the void defect in panel (b): (c) cobalt signal, (d) zinc signal, and (e) oxygen signal.

presence within the void except for some aggregates with low (poorly mixed) Zn content. The ZnO layer is of quite variable thickness, 10–20 nm thick.

HRTEM of the cross-section specimen, shown in Fig. 6, agrees with the XRD in showing a high proportion of crystallographically well-ordered material within the films. From the image contrast in HRTEM Fig. 6(a), we can resolve the crystal structure atop the amorphous SiO_x substrate, with the surface of this crystal disrupted by a lower-Z (presumably oxide) layer, which has a more granular microstructure. The patches of slightly darker contrast in this image could arise from either small variations in the lamella thickness or Ga contamination from the lamella preparation. They are not confined to the film: they are also present in the substrate, as can be seen in Fig. 6(a).

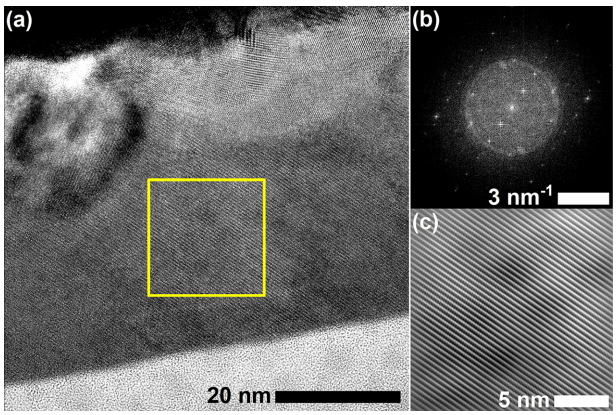

FIG. 6. High-resolution TEM of a sample grown with 24:25-W Co:Zn. (a) HRTEM image. Despite the voids prevalent throughout the sample, there is extensive crystalline material of 10–120-nm lateral dimensions throughout. (b) A fast Fourier transform taken centrally from the indicated region in (a), in which the bright spots relate to the crystalline periods present, while the diffuse circle is the disordered/amorphous material (chiefly due to the presence of the SiO_x substrate). (c) Inverse fast Fourier transform image of (b), clearly showing the visible lattice fringes.

Figure 6(c) shows an image from the central region of the large crystallite in Fig. 6(a); in preparing this image, brightness (contrast) and the maximum (minimum) thresholds were adjusted in Fourier space in order to better visualize the lattice fringes of the (110) planes in the β-Mn structure. Figure 6(b) is the fast Fourier transform of the central region of Fig. 6(a), showing the frequency-space response with clear crystalline periodicity overlaid with some contaminant peaks (likely to arise from the ZnO cap) and an amorphous circle from the inclusion of the SiO_x substrate.

Evidently, while the XRD pattern from the 24-W Co sample shows strong (221) β-Mn texture, the STEM reveals large voids and a thick ZnO cap that blankets the film, arising from the excessive Zn content. We therefore turn our attention now to a film with a higher Co content. Figure 7 shows STEM analysis of a cross-section cut from an annealed 36:25-W Co:Zn alloy sample. Comparing the HAADF-STEM contrast, shown in Fig. 7(a), with EDXS mapping, displayed in Figs. 7(b)–7(d), we can see that this film consists of CoZn sitting on the silica surface of the substrate with oxidized excess zinc at the surface. In the case of Fig. 7 this oxide layer is much reduced for the 36:25-W Co:Zn over the 24:25-W Co:Zn example in Figs. 6(a) and 5(b)–5(e) due to the correction to the as-deposited element ratios. It is also much more uniform, being 5 ± 1-nm thick. This reduction in ZnO is consistent with the XRD data presented in Fig. 4(b).

EDXS results for Co:Zn ratios give a composition of approximately 57 ± 4 at.% Zn to 43 ± 4 at.% Co for 24:25 W, and approximately 54 ± 3.67 at.% Zn to 46 ± 4 at.% Co 36:25 W. The measurement region was confined to the nominally CoZn layer. These values are within expectations for the stoichiometry of β-Mn phase CoZn alloy, based on the bulk phase diagram [40].

The example shown in the HAADF-STEM image in Fig. 7(a) contains two fairly significant surface crystallites of ZnO, making tracking of the responsible elements in the

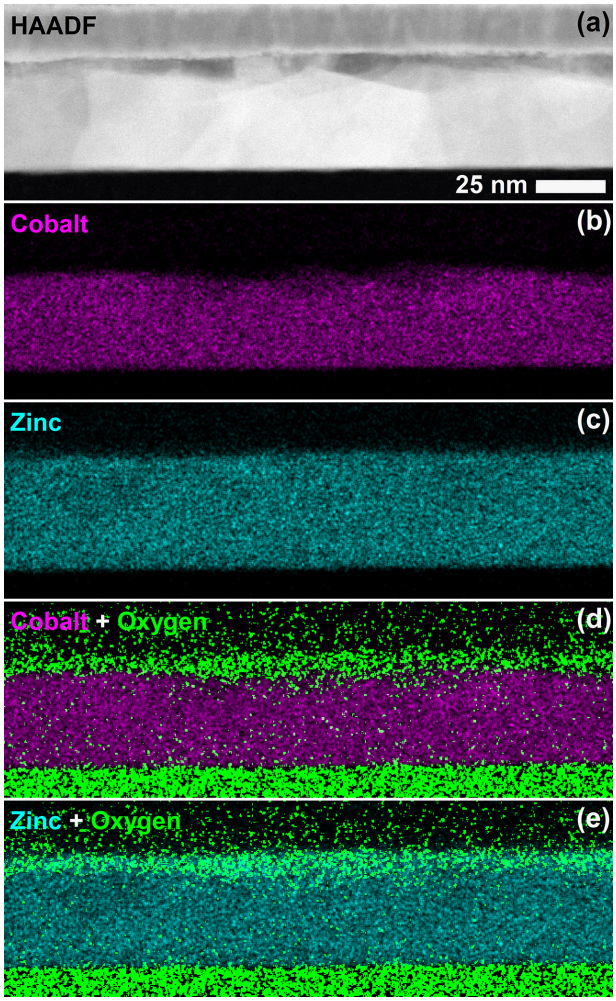

FIG. 7. STEM/EDXS analysis of an annealed 36:25-W Co:Zn alloy sample (approximately $416 \pm 6 -$ Å thick). (a) HAADF-STEM image of EDXS scan region. (b) Cobalt element signal. (c) Zinc element signal. (d) Oxygen element signal superimposed over the Co signal. (e) Oxygen element signal superimposed over the Zn signal. There exists only a small Zn oxide layer atop the film, which is distinct from the CoZn film.

corresponding EDXS maps in Figs. 7(b)–7(e) easy. From these maps, one can clearly see that the portion of the sample containing Co is distinct from the oxide portion. However, this is not the case for Zn, which overlaps with Co for most of the film thickness but also with O in a thin layer at the top. We can therefore conclude that most of the film is metallic CoZn with a thin ZnO cap.

Figure 8(a) shows a BF image of the whole film stack for the 36:25-W Co:Zn sample, which is close to the optimal composition ratio. Figures 8(b)–8(d) summarize dark-field (DF) imaging. DF imaging allows us to image parts of the sample that give rise to specific diffraction peaks within the reciprocal-space diffraction pattern, Fig. 8(b). This results in an orientation-specific contrast shift, allowing us to view all similarly aligned crystals.

In Fig. 8(b), which shows a diffraction pattern taken at near-normal incidence to the lamella, we can see from the large number of diffraction spots present that there is a variety of crystal orientations visible. Given the electron beam's spot size, which overlaps the amorphous SiO_x and even the Si beneath even that, many diffraction features arise from those regions. However, the contributions from the CoZn film are easily identifiable, and on aligning to them, DF imaging results in several large crystallites being readily apparent. Both of the examples given in Figs. 8(c) and 8(d) are over 200 nm in lateral dimension, and have minimal zinc oxide contaminating the surface. It is plausible that the different orientations for these crystallites revealed by this DF imaging is the reason for the XRD peak intensity seen for films sputtered with Co powers close to 36 W being reduced when compared to films with lower powers that show more intense XRD peaks.

C. Magnetic properties

The magnetic properties of a second series of films prepared in nominally the same way were measured by SQUID-VSM. Small uncontrolled differences in the deposition conditions with respect to the previous set of samples mean that the composition achieved for a given Co power was found to have shifted slightly, elucidated by comparing XRD data as described in the Appendix. Hence, for ease of comparison, we discuss these samples in terms of effective Co deposition powers in this section. These effective powers are $\sim 1.16\times$ higher than the measured experimental sputter power. All of our CoZn films display T_C above room temperature,

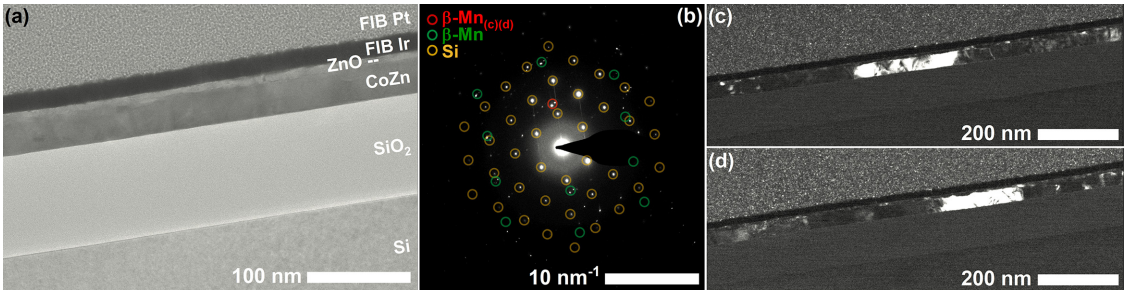

FIG. 8. TEM imaging of an annealed sample of 36:25-W Co:Zn. (a) BF image with variations in contrast indicative of differences in Z contrast of the different elements involved. (b) Reciprocal-space diffraction pattern, showing a combination of Si, SiO_x, and β-Mn structure CoZn signals, identified by differently colored circles, from which (c) and (d) were selected. (c,d) DF imaging of the 36:25-W Co:Zn alloy sample from an alignment to β-Mn CoZn peaks in the reciprocal diffraction pattern of (b). These show large platelike crystallites, over 200 nm in lateral dimension.

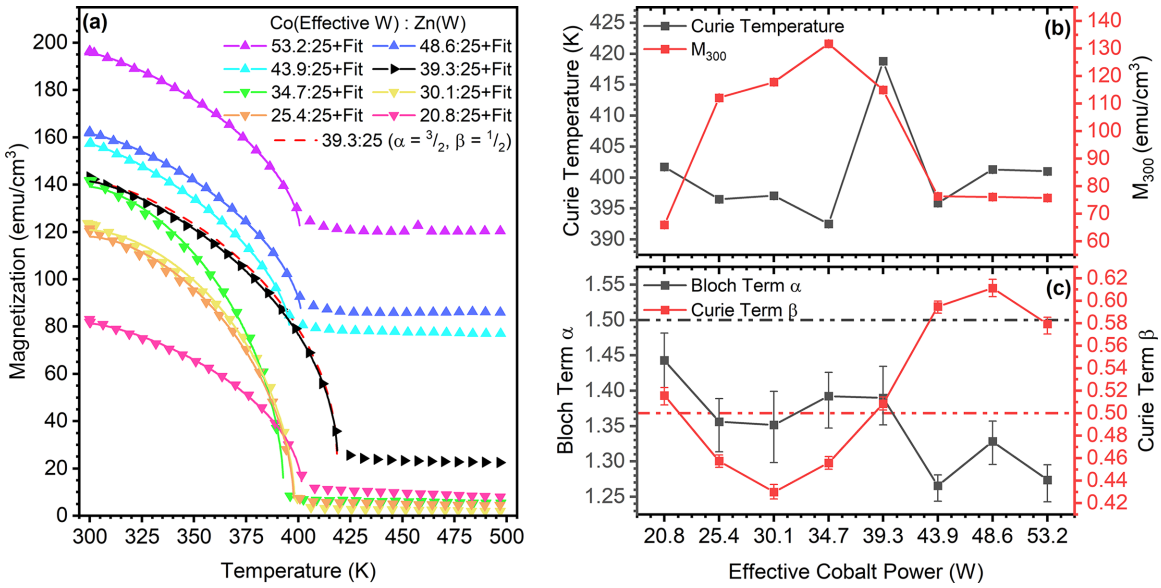

FIG. 9. Temperature-dependent magnetic measurements of annealed sputtered CoZn thin films. (a) $M(T)$ results for the CoZn films deposited at effective growth-power ratios of 20.8–53.2:25-W (22–50:25) Co:Zn, where Co powers are effective values to allow easier comparison with prior data. Data points represent experimental results; the solid line shows the result of fitting, as described in the text. The extent of the solid line shows the region that was fitted. (b) T_C and M_{300} vs composition. (c) Empirical Curie-Bloch fitting exponents α and β vs composition, with the ideal values of $\alpha = \frac{3}{2}$ and $\beta = \frac{1}{2}$ given by the dashed lines.

as shown in the magnetization versus temperature curves of Fig. 9(a). In most cases, the value of T_C lies between 390–405 K. However, close to the structurally optimal composition ratio (of 40:25-W Co:Zn as determined by XRD shown in Fig. 4 and STEM/EDXS shown in Fig. 7), there is a significant jump to a higher T_C of approximately 420 K, shown in Fig. 9(a) and summarized in Fig. 9(b), where we plot T_C as a function of Co deposition power. This value is comparable to bulk values [10,14,22].

Further examination of Fig. 9(a) shows that the magnetization retains a substantial value above T_C for Co content higher than this optimal value. Even at the structurally optimal composition there remains some modest level of retained background magnetism above T_C. This is likely to arise from the development of Co-rich aggregates, which remain ferromagnetic to much higher temperatures: the bulk T_C of Co is ∼1400 K. We do not observe any XRD peaks associated with any such aggregates in Fig. 4, which suggests that they must be too small to present a meaningful diffraction volume. It can be shown that the volume fraction of the film occupied by these aggregates can be estimated as $x = M_{500}/M_{Co}$, where M_{500} is the retained magnetization (which we take to be the magnetization measured at 500 K) and $M_{Co} = 1400$ emu/cm^3 is the bulk magnetization of Co. Up to and including the 39.3:25-W Co:Zn sample, $x = 1\%$ or less, and rises to ∼9% for the 53.2:25-W Co:Zn sample.

These $M(T)$ curves below the T_C of the CoZn were fitted with the empirical approximation to Bloch's law for the ferromagnetic phase given by Eq. (1). All curves had a linear background subtraction applied based on the above-T_C magnetization prior to fitting. Hence, we define M_{300} as the magnetization of the CoZn film, i.e., above the background level, at 300 K.

Fitting of the $M(T)$ curve shows a few interesting features beyond the spike seen in T_C just above the optimal composition ratio. Figure 9(b) also shows the room-temperature magnetization M_{300} to have a region of elevated values ∼120 emu/cm^3 specifically between our case of strong crystallinity in XRD at 25.4:25-W Co:Zn to just the compositional optimum seen around 39.3:25-W Co:Zn. Indeed, the very highest value for M_{300} matches that optimal power ratio. Beyond this limit the room-temperature magnetization drops to approximately 75 emu/cm^3. We interpret this as meaning that the remainder of the film can become somewhat depleted in Co as the Co-rich aggregates form.

In Fig. 9(c) we show the Bloch and Curie exponents α and β. In a simple ferromagnet, spin-wave theory predicts that $\alpha = \frac{3}{2}$, which is known as the Bloch law, and is valid at temperatures well below T_C. We do not have data here that are strictly in that regime, but nevertheless, the values of α that were returned by our fit are not far below this value.

Meanwhile, β is a critical exponent that has a value $\frac{1}{2}$ according to a simple Landau model of the ferromagnetic phase transition. We find values close to this, especially near the optimal composition of 39.3:25-W Co:Zn.

The fact that our measured values of α and β are not far from the ideal ones tells us that that our material is fairly well described as a conventional three-dimensional ferromagnet. The way that the values start to depart from the ideal values for Co deposition powers of 43.9 W and higher can possibly be attributed to the CoZn coupling to the nanoscale Co-rich aggregates that give rise to the magnetic background for these samples.

Figures 10(a)–10(c) show hysteresis loops measured using an in-plane field for selected samples from the series for which data were shown in Fig. 9. In each panel, data taken

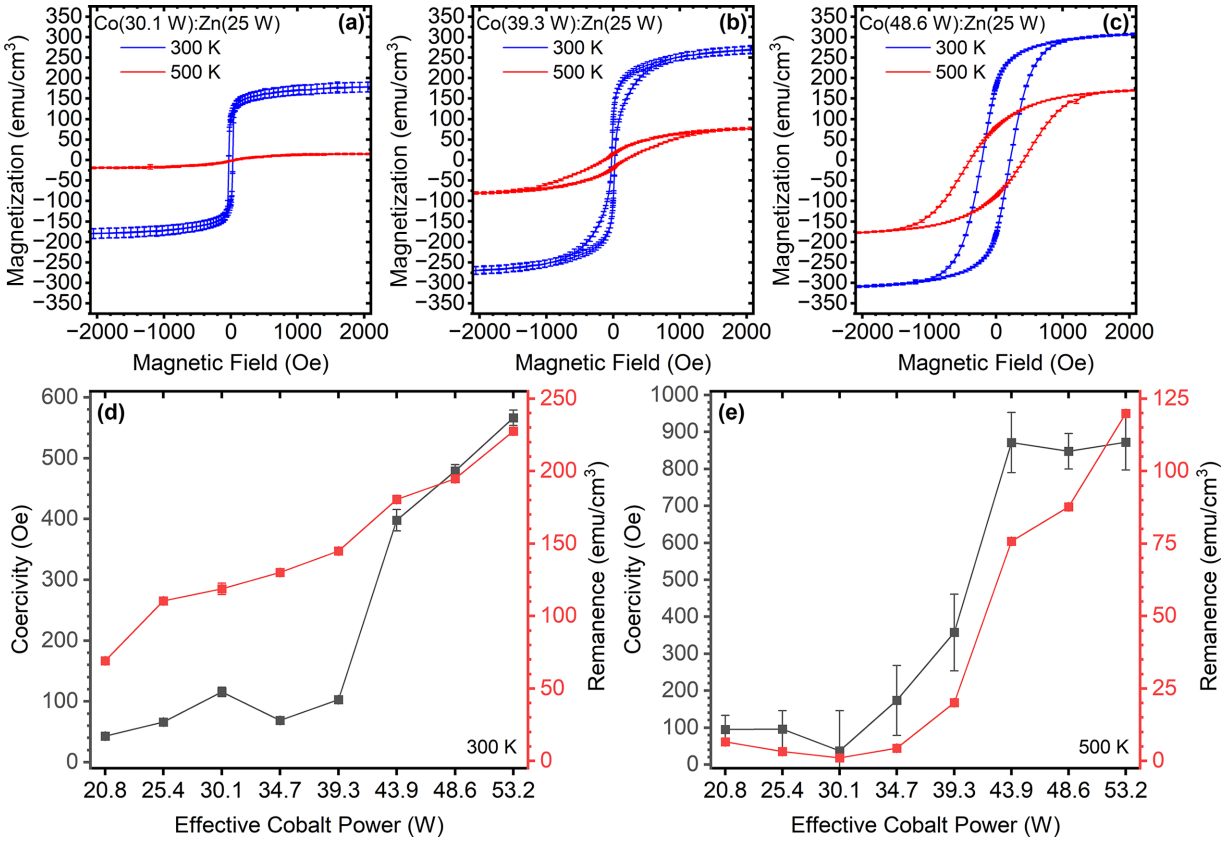

FIG. 10. Magnetic hysteresis loops. (a)–(c) Loops taken under in-plane magnetic field at 300 and 500 K for selected samples, labeled by effective growth powers. Summary of coercivity and remanence results for whole series of samples at: (d) 300 K and (e) 500 K.

at 300 K (close to room temperature) and 500 K (above the CoZn Curie temperature) are shown. In Fig. 10(a), for the effective 30.1:24-W Co:Zn, we see little hysteresis or magnetization at 500 K, while typical soft ferromagnetic behavior at 300 K is shown. Figure 10(b) shows the hysteresis for the sample displaying an elevated T_C in Fig. 9; while still of low coercivity, at 300 K the hysteresis above the CoZn T_C is already beginning to show a harder ferromagnetic behavior developing (due to improperly integrated Co in the alloy).

Meanwhile, in Fig. 10(c) there is clear and substantial ferromagnetic hysteresis at 500 K as well as 300 K, albeit with a reduced moment at the higher temperature. We interpret this as the hysteresis of the Co-rich aggregates. The substantially higher 300 K coercive field at this higher effective Co power can be attributed to the CoZn in this film being coupled to the magnetically much harder Co-rich aggregates.

In Fig. 10(d) we present data for the coercive field and remanence for this entire second series of samples. The remanence rises approximately linearly as the Co content of the film increases, as expected. Meanwhile, there is a significant jump to higher values of coercivity for the three most Co-rich films, those three for which Fig. 9 shows a significant residual magnetization above the Curie point of the CoZn, owing to the hardening of the CoZn by the nanoscale Co-rich aggregates.

Meanwhile, Fig. 10(e) shows the same two quantities for the same series of samples at 500 K, above the Curie point of the CoZn. Up to the optimal effective power of 39.3:24-W Co:Zn, both coercive field and remanence are small or even negligible, as expected. There is then a rapid rise as the Co-rich aggregates begin to form, with the three highest Co samples having a substantial coercive field of ∼900 Oe and a remanence of ∼100 emu/cm^3 owing to the presence of the Co-rich aggregates that remain magnetic at this elevated temperature.

IV. CONCLUSION

To summarize the results, the XRD shows that codeposited films of CoZn annealed up to 400 °C have a stable state of β-Mn phase over a wide range of sputtered composition ratios. The resulting phase prevails due to the high mobility of zinc at low temperatures. The limiting factors appear to be cases where the composition is exceptionally high in one or the other of the two elements. In the case of high zinc content we are limited by the vapor pressure and annealing temperature of the films leading to voids and a substantial ZnO cap, and in the case of high cobalt content we are limited by the accrual of cobalt-rich aggregates. Our results can act as guidelines on how to achieve optimal-quality sputtered CoZn films, balancing these two undesirable outcomes, and are likely to have bearing on other alloy thin film growth processes where one component has a very high vapor pressure.

While ∼24 W deposition power for cobalt shows the strongest β-Mn crystalline response by XRD, it was observed by electron microscopy that these films were full of voids, as well as possessing the thick ZnO cap. In fact, ∼36 W

deposition power for cobalt led to a better volume fraction of β-Mn CoZn with a much more uniform film.

Crystallinity within the films appears limited, with grains not observed to grow above ∼200 nm in plane, regardless of annealing time. The mechanisms responsible for this are unknown, but it is proposed that due to zinc having a high affinity for oxygen binding and alloy formation that contamination from the vacuum could be an issue. Alternatively, this could be a mechanical restriction based on the diffusion of the elements close to stoichiometry, or limited by energetic requirements to rearrange masses of metastable crystallites.

Annealed films of cosputtered CoZn of β-Mn phase are ferromagnetic at and above above room temperature. Around the optimal composition by volume ratio (39.3–41.6-W Co deposition power), a higher T_C than the rest of the series that show good β-Mn crystalline structure is obtained. For higher Co deposition powers we observed a weakly temperature-dependent background magnetization that we attribute to excess Co precipitating out into nanoscale aggregates.

Both the room-temperature magnetization and the T_C of thin films close to the optimal composition of Co:Zn to give a sample that is effectively entirely in the β-Mn phase compare well with the bulk-crystal literature results of Tokunaga *et al.* (2015) [10]. The positive comparison of these features, and the expectation that the magnetic phase diagram would follow the template of the B20 materials [5,6], leads to the potential for these films to also support chiral magnetic textures. Our results suggest that attempts at epitaxial growth and to seek chiral magnetism are fruitful future directions for research.

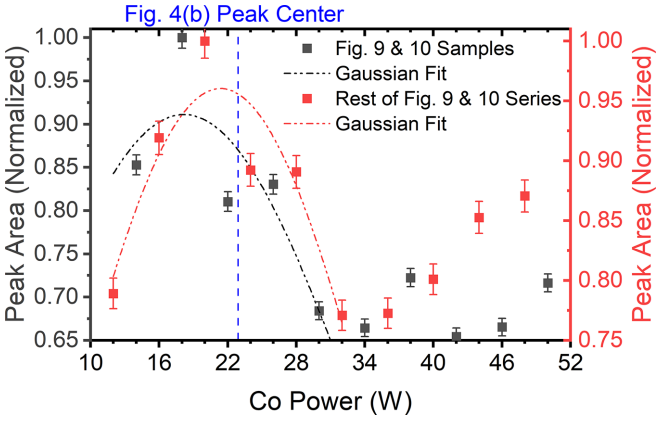

FIG. 11. ZnO (0002)-normalized XRD peak area as a function of Co sputter power for the second series of samples. Black data points are for the same samples as Fig. 9 and Fig. 10, while red are the alternating samples from the same growth series but annealed in a separate ampule (under nominally identical temperature conditions, but perhaps an unintended variation in vacuum quality). Dashed-dotted lines show a Gaussian fitted to the data points at lower powers where there is a peak in normalized XRD peak area with Co power. Peak centers are 18.24 W (black) and 21.42 W (red); the position of the equivalent peak for the data shown in Fig. 4(b) is marked with a blue dashed line.

ACKNOWLEDGMENTS

We would like to thank Dr. Gavin Stenning and Dr. Daniel Nye for help on the Rigaku Smartlab and Quantum Design MPMS3 SQUID-VSM instruments in the Materials Characterisation Laboratory at the ISIS Neutron and Muon Source. We would like to thank Mr. John Harrington and Dr. Zabeada Aslam for help on the Helios G4 DualBeam FIB and Titan3 electron microscope instruments at the Leeds Electron Microscopy and Spectroscopy Centre. This work was supported in part by the ISIS Facility Development Studentship scheme.

DATA AVAILABILITY

The data that support the findings of this article are openly available [41].

APPENDIX: COMPARING SPUTTER DEPOSITION POWER

In this paper we compare two series of thin-film samples in which the Co:Zn stoichiometry was varied by fixing the Zn sputter power and varying the Co sputter power. Defining the exact stoichiometry of the deposited film is not straightforward owing to the differential oxidation of the Zn and the formation of Co-rich precipitates, so we prefer to present our data in terms of the sputter powers used that are measured and well defined.

The first series of samples was subjected to a detailed structural characterization including XRD, SEM, and TEM analysis, presented in Secs. III A and III B, while the second series was subjected to a detailed magnetic characterization, presented in Sec. III C.

Nevertheless, the two series of samples were grown several months apart and so there are small differences in the deposition rates for a given sputter power, which lead to small shifts in stoichiometry. To facilitate easier comparison for the reader of the two sets of samples, we have chosen to present the data in Sec. III C in terms of an effective Co power so that numerical values labeling particular samples are as close a match as possible to the set of samples for which we present the structural data.

The effective powers for the second series of samples are defined as ∼1.16× higher than the actual experimental deposition power. The size of this shift is based on comparison of XRD taken from the second series of samples with the equivalent data for the first series that is shown in Fig. 4. As an example, in Fig. 11 we show XRD data in a similar manner as Fig. 4(b). There, data points for samples for which magnetic data appear in Figs. 9 and 10 are shown using black data points. These samples were selected from a longer growth series that was annealed in an alternating series of growth-power steps; hence, there are further samples for which we show the XRD data using red data points in Fig. 11. As such, this entire series should represent a complete stoichiometric variation series with differences due to the annealing environment. For each series we fitted a Gaussian to the regime where we see elevated normalized XRD peak area for the ZnO (0002) reflection, shown with dashed-dotted lines, which can be compared with the position of an equivalent Gaussian fitted to the data in Fig. 4(b), shown by a blue dashed line, which is for slightly higher Co power. As these series show the same expected trend in peak area, we use both to define the

scaling factor given above for the effective Co power for this series of samples. Note, this scaling factor is also absorbing the contribution from the Zn growth-rate change (error), but as this trend is stoichiometry based we believe it is appropriate.

[1] A. Fert, V. Cros, and J. Sampaio, Skyrmions on the track, Nat. Nanotechnol. **8**, 152 (2013).

[2] G. Finocchio, F. Büttner, R. Tomasello, M. Carpentieri, and M. Kläui, Magnetic skyrmions: From fundamentals to applications, J. Phys. D: Appl. Phys. **49**, 423001 (2016).

[3] C. H. Marrows and K. Zeissler, Perspective on skyrmion spintronics, Appl. Phys. Lett. **119**, 250502 (2021).

[4] A. N. Bogdanov and D. A. Yablonskii, Thermodynamically stable "vortices" in magnetically ordered crystals. The mixed state of magnets, Sov. Phys. JETP **68**, 101 (1989).

[5] S. Mülbauer, B. Binz, F. Jonietz, C. Pfleiderer, A. Rosch, A. Neubauer, R. Georgii, and P. Böni, Skyrmion lattice in a chiral magnet, Science **323**, 915 (2009).

[6] X. Z. Yu, Y. Onose, N. Kanazawa, J. H. Park, J. H. Han, Y. Matsui, N. Nagaosa, and Y. Tokura, Real-space observation of a two-dimensional skyrmion crystal, Nature (London) **465**, 901 (2010).

[7] X. Z. Yu, N. Kanazawa, Y. Onose, K. Kimoto, W. Z. Zhang, S. Ishiwata, Y. Matsui, and Y. Tokura, Near room-temperature formation of a skyrmion crystal in thin-films of the helimagnet FeGe, Nat. Mater. **10**, 106 (2011).

[8] S. Seki, X. Z. Yu, S. Ishiwata, and Y. Tokura, Observation of skyrmions in a multiferroic material, Science **336**, 198 (2012).

[9] N. Kanazawa, S. Seki, and Y. Tokura, Noncentrosymmetric magnets hosting magnetic skyrmions, Adv. Mater. **29**, 1603227 (2017).

[10] Y. Tokunaga, X. Z. Yu, J. S. White, H. M. Rønnow, D. Morikawa, Y. Taguchi, and Y. Tokura, A new class of chiral materials hosting magnetic skyrmions beyond room temperature, Nat. Commun. **6**, 7638 (2015).

[11] K. Buschow, P. van Engen, and R. Jongebreur, Magneto-optical properties of metallic ferromagnetic materials, J. Magn. Magn. Mater. **38**, 1 (1983).

[12] T. Hori, H. Shiraish, and Y. Ishii, Magnetic properties of β-Mn CoZn alloys, J. Magn. Magn. Mater. **310**, 1820 (2007).

[13] O. Karlsen, A. Kjekshus, H. Fjellvåg, P. Ravindran, R. Vidya, and B. Hauback, Structure and magnetism of the β-Mn-Co solid-solution phase, J. Alloys Compd. **476**, 9 (2009).

[14] W. Xie, S. Thimmaiah, J. Lamsal, J. Liu, T. W. Heitmann, D. Quirinale, A. I. Goldman, V. Pecharsky, and G. J. Miller, β-Mn-type $Co_{8+x}Zn_{12-x}$ as a defect cubic laves phase: Site preferences, magnetism, and electronic structure, Inorg. Chem. **52**, 9399 (2013).

[15] J. K. Cockcroft, *A Hypertext Book of Crystallographic Space Group Diagrams and Tables* (Department of Crystallography, Birkbeck College, University of London, London, 1999).

[16] J. Donohue, *The Structures of the Elements* (John Wiley & Sons, New York, 1974), pp. 191–199.

[17] K. Karube, J. S. White, N. Reynolds, J. L. Gavilano, H. Oike, A. Kikkawa, F. Kagawa, Y. Tokunaga, H. M. Rønnow, Y. Tokura, and Y. Taguchi, Robust metastable skyrmions and their triangular-square lattice structural transition in a high-temperature chiral magnet, Nat. Mater. **15**, 1237 (2016).

[18] K. Karube, J. S. White, D. Morikawa, M. Bartkowiak, A. Kikkawa, Y. Tokunaga, T. Arima, H. M. Rønnow, Y. Tokura, and Y. Taguchi, Skyrmion formation in a bulk chiral magnet at zero magnetic field and above room temperature, Phys. Rev. Mater. **1**, 074405 (2017).

[19] R. Takagi, D. Morikawa, K. Karube, N. Kanazawa, K. Shibata, G. Tatara, Y. Tokunaga, T. Arima, Y. Taguchi, Y. Tokura, and S. Seki, Spin-wave spectroscopy of the Dzyaloshinskii-Moriya interaction in room-temperature chiral magnets hosting skyrmions, Phys. Rev. B **95**, 220406(R) (2017).

[20] D. Morikawa, X. Yu, K. Karube, Y. Tokunaga, Y. Taguchi, T.-H. Arima, and Y. Tokura, Deformation of topologically-protected supercooled skyrmions in a thin plate of chiral magnet $Co_8Zn_8Mn_4$, Nano Lett. **17**, 1637 (2017).

[21] K. Karube, J. S. White, D. Morikawa, C. D. Dewhurst, R. Cubitt, A. Kikkawa, X. Yu, Y. Tokunaga, T.-h. H. Arima, H. M. Rønnow, Y. Tokura, and Y. Taguchi, Disordered skyrmion phase stabilized by magnetic frustration in a chiral magnet, Sci. Adv. **4**, eaar7043 (2018).

[22] J. D. Bocarsly, C. Heikes, C. M. Brown, S. D. Wilson, and R. Seshadri, Deciphering structural and magnetic disorder in the chiral skyrmion host materials $Co_xZn_yMn_z$ $(x + y + z = 20)$, Phys. Rev. Mater. **3**, 014402 (2019).

[23] G. Chen, A. Mascaraque, A. T. N'Diaye, and A. K. Schmid, Room temperature skyrmion ground state stabilized through interlayer exchange coupling, Appl. Phys. Lett. **106**, 242404 (2015).

[24] W. Jiang, P. Upadhyaya, W. Zhang, G. Yu, M. B. Jungfleisch, F. Y. Fradin, J. E. Pearson, Y. Tserkovnyak, K. L. Wang, O. Heinonen, S. G. E. Velthuis, and A. Hoffmann, Blowing magnetic skyrmion bubbles, Science **349**, 283 (2015).

[25] C. Moreau-Luchaire, C. Moutafis, N. Reyren, J. Sampaio, C. A. Vaz, N. Van Horne, K. Bouzehouane, K. Garcia, C. Deranlot, P. Warnicke, P. Wohlhüter, J. M. George, M. Weigand, J. Raabe, V. Cros, and A. Fert, Additive interfacial chiral interaction in multilayers for stabilization of small individual skyrmions at room temperature, Nat. Nanotechnol. **11**, 444 (2016).

[26] S. Woo, K. Litzius, B. Krüger, M. Y. Im, L. Caretta, K. Richter, M. Mann, A. Krone, R. M. Reeve, M. Weigand, P. Agrawal, I. Lemesh, M. A. Mawass, P. Fischer, M. Kläui, and G. S. Beach, Observation of room-temperature magnetic skyrmions and their current-driven dynamics in ultrathin metallic ferromagnets, Nat. Mater. **15**, 501 (2016).

[27] O. Boulle, J. Vogel, H. Yang, S. Pizzini, D. de Souza Chaves, A. Locatelli, T. O. Menteş, A. Sala, L. D. Buda-Prejbeanu, O. Klein, M. Belmeguenai, Y. Roussigné, A. Stashkevich, S. M. Chérif, L. Aballe, M. Foerster, M. Chshiev, S. Auffret, I. M. Miron, and G. Gaudin, Room-temperature chiral magnetic skyrmions in ultrathin magnetic nanostructures, Nat. Nanotechnol. **11**, 449 (2016).

[28] A. Soumyanarayanan, M. Raju, A. L. Gonzalez Oyarce, A. K. C. Tan, M.-Y. Im, A. P. Petrović, P. Ho, K. H. Khoo, M. Tran, C. K. Gan, F. Ernult, and C. Panagopoulos, Tunable

room-temperature magnetic skyrmions in Ir/Fe/Co/Pt multilayers, Nat. Mater. **16**, 898 (2017).

[29] K. Zeissler, S. Finizio, K. Shahbazi, J. Massey, F. A. Ma'Mari, D. M. Bracher, A. Kleibert, M. C. Rosamond, E. H. Linfield, T. A. Moore, J. Raabe, G. Burnell, and C. H. Marrows, Discrete Hall resistivity contribution from Néel skyrmions in multilayer nanodiscs, Nat. Nanotechnol. **13**, 1161 (2018).

[30] Z. Li, X. Mi, X. Wang, J. Lyu, N. Su, A. Wang, Y. Chai, B. Yuan, W. Luo, H. Cheng, J. Gao, H. Wang, L. Hao, M. He, J. Shen, Y. Sun, and X. Tong, Pressure tunable magnetic skyrmion phase in $Co_8Zn_8Mn_4$ single crystals, arXiv:2402.14477.

[31] K. Momma and F. Izumi, VESTA 3 for three-dimensional visualization of crystal, volumetric and morphology data, J. Appl. Crystallogr. **44**, 1272 (2011).

[32] *CRC Handbook of Chemistry and Physics*, 97th ed., edited by W. M. Haynes, D. R. Lide, and T. J. Bruno (CRC Press, Taylor & Francis Group, Boca Raton, FL, 2016).

[33] C. L. Yaws, *Yaws' Handbook of Antoine Coefficients for Vapor Pressure*, 2nd ed. (Knovel, Beaumont, TX, 2009).

[34] R. B. Heller, J. McGannon, and A. H. Weber, Precision determination of the lattice constants of zinc oxide, J. Appl. Phys. **21**, 1283 (1950).

[35] M. H. F. Overwijk, Novel scheme for the preparation of transmission electron microscopy specimens with a focused ion beam, J. Vac. Sci. Technol. B Microelectron. Nanom. Struct. **11**, 2021 (1993).

[36] R. M. Langford and M. Rogers, *In situ* lift-out: Steps to improve yield and a comparison with other FIB TEM sample preparation techniques, Micron **39**, 1325 (2008).

[37] M. Schaffer, B. Schaffer, and Q. Ramasse, Sample preparation for atomic-resolution STEM at low voltages by FIB, Ultramicroscopy **114**, 62 (2012).

[38] R. F. L. Evans, U. Atxitia, and R. W. Chantrell, Quantitative simulation of temperature-dependent magnetization dynamics and equilibrium properties of elemental ferromagnets, Phys. Rev. B **91**, 144425 (2015).

[39] Zn power was chosen to be 25 W based on separate atomic force microscope studies that showed minimum film roughness at this power.

[40] *ASM Handbook, Volume 3, Alloy Phase Diagrams*, edited by H. Baker, H. Okamoto, and S. D. Henry (ASM International, Materials Park, Ohio, 1992).

[41] M. Dearg, G. Burnell, S. Langridge, and C. H. Marrows, Research Data Leeds (2025), https://doi.org/10.5518/1715.